

Mass-independent scheme for enhancing spatial quantum superpositionsRun Zhou ¹, Ryan J. Marshman ², Sougato Bose,³ and Anupam Mazumdar ¹¹*Van Swinderen Institute, University of Groningen, 9747 AG Groningen, The Netherlands*²*Centre for Quantum Computation and Communication Technology, School of Mathematics and Physics, University of Queensland, Brisbane, Queensland 4072, Australia*³*Department of Physics and Astronomy, University College London, Gower Street, WC1E 6BT London, United Kingdom*

(Received 8 November 2022; revised 11 January 2023; accepted 23 February 2023; published 16 March 2023)

Placing a large mass in a large spatial superposition, such as a Schrödinger cat state, is a significant and important challenge. In particular, the large spatial superposition [$O(10\text{--}100)$ μm] of mesoscopic masses [$m \sim O(10^{-14}\text{--}10^{-15})$ kg] makes it possible to test the quantum nature of gravity via entanglement in the laboratory. To date, the proposed methods of achieving this spatial delocalization are to use wave-packet expansions or quantum ancilla- (for example, spin-) dependent forces, all of whose efficacy reduces with mass. Thus increasing the spatial splitting independently of the mass is an important open challenge. In this paper we present a method of achieving a mass-independent enhancement of superposition via diamagnetic repulsion from current-carrying wires. We analyze an example system which uses the Stern-Gerlach effect to creating a small initial splitting and then apply our diamagnetic repulsion method to enhance the superposition size $O(400\text{--}600)$ μm from an initial modest split of the wave function. We provide an analytical and numerical analysis of our scheme.

DOI: [10.1103/PhysRevA.107.032212](https://doi.org/10.1103/PhysRevA.107.032212)**I. INTRODUCTION**

Gravity is special as it is not yet evident whether gravity is a classical or a quantum entity [1]. It is often thought that any quantum gravitational effects will become important only when we approach the Planck length or the timescale, making it impossible to probe directly. Furthermore, cosmological data, such as perturbations in the cosmic microwave background radiation [2] and the potential B modes for future detection, may not help to settle this outstanding issue [3]. Both astrophysical and cosmological sources contain many uncertainties [4].

Despite all these challenges, a tabletop experiment has recently been proposed to explore the quantum origin of gravity with the help of quantum superposition and quantum entanglement in the infrared [5–7] (see also [8,9]). The protocol is known as the quantum gravity-induced entanglement of masses (QGEM), which evidences both the quantum superposition of geometries [10,11] and the exchange of virtual gravitons [6], that is, spin-2 graviton exchange [7] (see also [12]). Recently, a protocol has been created to entangle the matter with that of the standard model photon in a gravitational optomechanical setup [13] (see also [14]). This will probe not only the light bending due to the gravitational interaction but also the spin-2 nature of the graviton-mediated entanglement [13]. Note that the entanglement is purely a quantum observable, which measures the quantum correlation in complementary bases, and has no classical analog whatsoever.

One of the key challenges towards realizing the QGEM protocol experimentally is to create a large spatial superposition $\delta z \sim O(10\text{--}100)$ μm for a large mass object [$m \sim O(10^{-14}\text{--}10^{-15})$ kg] (for details see [5,15] and for a free-falling setup see [5,16]). It is also well known that creating

a large superposition has many further fundamental applications; one can test the foundations of quantum mechanics in the presence of gravity [17–21], a purely quantum gravitational version of the equivalence principle [22], falsifying spontaneous collapse mechanisms [19,20], placing a bound on decoherence mechanisms [23–29], quantum sensors [16,30], probing the physics of a fifth fundamental force and the axion [31], and probing gravitational waves [30].

Atom interferometers are well known to create a large baseline superposition [32–34], but at masses well below what is required to test the quantum nature of gravity. To date, macromolecules represent the heaviest masses placed in a superposition of spatially distinct states [35,36]. There are physical schemes to obtain tiny superpositions of large masses [37] or moderate-size (approximately 10 nm to 1 μm) superpositions of approximately $10^{-19}\text{--}10^{-17}$ kg masses [24,25,38–49]. However, we require a large spatial superposition of heavy [$m \sim O(10^{-17}\text{--}10^{-14})$ kg] masses, with the current likely scheme utilizing the Stern-Gerlach effect [50–55]. In fact, a proof of principle experiment has already been conducted using atoms, showing that such a Stern-Gerlach interferometer for massive objects can indeed be realized [53].

The crucial problem now is how to achieve a large spatial separation for these larger mass particles. There are so far only two realistic types of schemes to separate wave packets, one using wave-packet expansions in conjunction with slits or measurements [24,35,36,45–49] and the other using spin-dependent forces [53–55]. However, both schemes inevitably become progressively worse as the mass increases. This paper presents a mass-independent experimental scheme to create a large spatial superposition.

There are already some very attractive experimental ideas which have been proposed to create large superposition

for masses in the range of $m \sim O(10^{-17}-10^{-14})$ kg (see Refs. [5,30,54–56]). References [54–56] considered the effect of induced magnetic potential in the diamondlike crystal along with the nitrogen-valence (NV) -centered potential. However, it was also noticed that the diamagnetic term in the Hamiltonian inhibits the spatial superposition despite taking into account that the coherence of the NV center can be maintained for a long enough time [54,56]. This was mainly due to the fact that the diamagnetic term creates a harmonic trap and the particle tends to move towards the center of the potential, therefore inhibiting the growth in the superposition size. This issue was tackled by employing new dynamical techniques such as catapulting the trajectory by assuming a nonlinear profile for the magnetic field [55]. In the present paper we explore the possibility of utilizing this unavoidable induced diamagnetic effect to enhance the superposition size. In our analysis we use the simple example model of a magnetic field sourced by current-carrying wires.

Our aim is to enhance the superposition size using only modest currents, but requires one simple assumption. We assume that we have already created an initial spatial superposition of the nanocrystal, as could be made using a Stern-Gerlach setup (see [54–56]). In particular, we take for demonstration the initial superposition size $\Delta z_0 \sim 1 \mu\text{m}$ and present how this can be increased to a size of $\Delta z \sim O(100-500) \mu\text{m}$. We also assume that the interferometer setup is one dimensional. In addition, once we create the superposition, we assume that the superposition can be closed using the same splitting mechanism, i.e., by the Stern-Gerlach mechanism (see [55]). It is for this reason we present this as an enhancement of a spatial superposition. We provide both analytical and numerical analyses. We take the modest currents to be approximately $O(1)$ A and restrict the example operating time to be within approximately 0.1's while still aiming to maximize the superposition size.

The maximum size of the superposition does not depend on the mass, thus making this an attractive scheme for creating a macroscopic quantum superposition for any range of masses, provided the initial small superposition is first created. We will show that there are two possible configurations: one where the trajectory is triangular and the other where the trajectory traces its path after interacting with the wire with a closest impact parameter, discussed below.

In our present analysis we assume that the nanocrystal is not rotating. Recent work has analyzed the rotation of the crystal in Refs. [57–59]. We will need revisit this issue separately once we fully analyze the largest superposition size we can obtain. This is similar to the spin coherence problem and will require a dedicated study. We will not discuss how to close the superposition as it is possible to employ the Stern-Gerlach technique to close the trajectory (see [55]). Another generic issue is the phonon vibration causing the decoherence (see [60]). We assume that the desired level of internal cooling can be obtained to mitigate the phonon-induced decoherence. Given that all these challenges can be tackled, we ask how large a spatial superposition we can achieve via the diamagnetic contribution.

The paper is organized as follows. In Sec. B we discuss the setup with the Hamiltonian. In Sec. III we discuss diamagnetic

repulsion. In Sec. IV we provide the analytical understanding of the interaction of the nanocrystal with the fixed wires. The analysis is very similar to the central potential problem in classical mechanics. In Sec. V we present and discuss our numerical results. In Sec. VI we will conclude our paper with a summary and discussion.

II. SETUP

The Hamiltonian of a diamond embedded in a spin in a magnetic field is [56,61]

$$\hat{H} = \frac{\hat{p}^2}{2m} + \hbar D \hat{S}^2 - \frac{\chi_\rho m}{2\mu_0} \mathbf{B}^2 - \hat{\boldsymbol{\mu}} \cdot \mathbf{B}, \quad (1)$$

where $\hat{\boldsymbol{\mu}} = -g\mu_B \hat{\mathbf{S}}$ is the spin magnetic moment, $g \approx 2$ is the Landé g factor, $\mu_B = \frac{e\hbar}{2m_e}$ is the Bohr magneton, $\hat{\mathbf{S}}$ is the spin operator, \hat{p} is the momentum operator, \mathbf{B} is the magnetic field, and m , \hbar , D , χ_ρ , and μ_0 are scalars representing the mass of the diamond, the reduced Planck constant, NV zero-field splitting, magnetic susceptibility, and vacuum permeability, respectively. By applying the microwave pulse with an appropriate resonance frequency, the electron spin in the diamond can be coupled with the nuclear spin and the spin–magnetic-field interaction can be ignored [62]. We assume that this has happened prior to the amplification of the superposition size.

Let us first consider the magnetic field generated by a current-carrying wire

$$\mathbf{B} = \frac{\mu_0 \mathbf{I} \times \mathbf{e}_r}{2\pi r}, \quad (2)$$

where \mathbf{I} is the current carried by a straight wire, r is the vertical distance from the wire to a point in space, and \mathbf{e}_r is the unit vector corresponding to the distance r . At this point, the potential energy of the diamond in the magnetic field is given by

$$U = -\frac{\chi_\rho m}{2\mu_0} \mathbf{B}^2 = \frac{1}{2} m \alpha \frac{I^2}{r^2}, \quad (3)$$

where $\alpha = -\frac{\chi_\rho \mu_0}{4\pi^2}$. Combining Eqs. (3) and (2), the acceleration of the diamond can be obtained as

$$\mathbf{a}_{\text{dia}} = -\frac{1}{m} \nabla U = \alpha \frac{I^2}{r^3} \mathbf{e}_r. \quad (4)$$

It can be seen from Eq. (4) that the acceleration caused by the diamagnetic effect [the third term in Eq. (1)] is mass independent. This means we can get the desired acceleration of a diamagnetic object by setting an appropriate distance between the object and the wire and an appropriate current flowing through the wire regardless of the mass of the object. This property provides the possibility of obtaining a large superposition size for a massive object. We will use the trajectory of a classical wave packet to represent the expectation value of the position of the wave packet.

III. DIAMAGNETIC REPULSION

The scheme of increasing the superposition size by diamagnetic repulsion is mainly divided into three steps.

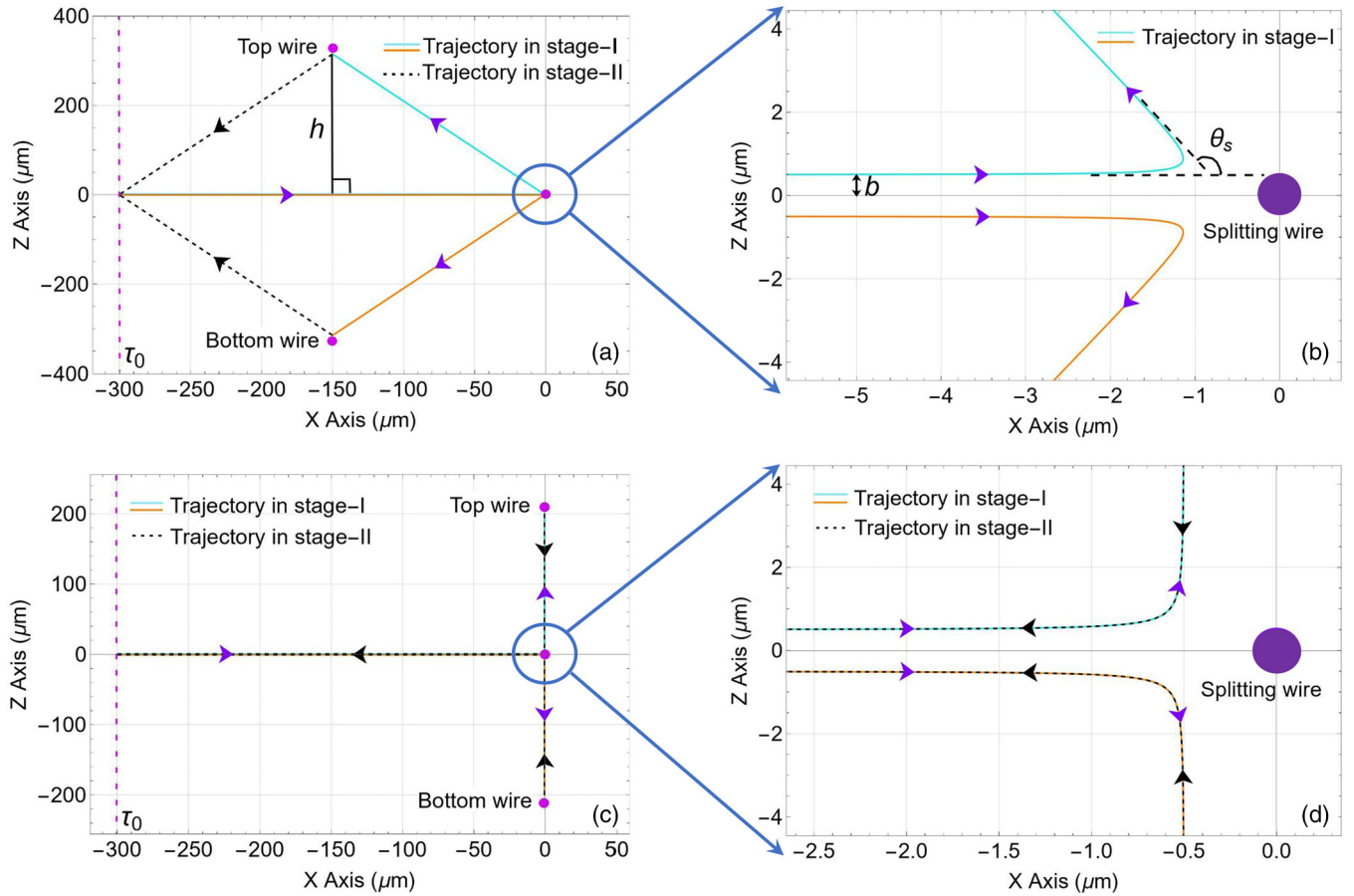


FIG. 1. Experimental scheme to create mass-independent superposition via diamagnetic repulsion. The wave packet comes out of the Stern-Gerlach interferometer at the moment τ_0 with an initial velocity v_0 parallel to the x axis (polar axis) and enters the magnetic field generated by the current-carrying wire. The purple points (circles) represent straight wires perpendicular to the x - z plane. The wire at the origin is called the splitting wire. The wire above the $z = 0$ axis is called the top wire and the wire below it is called the bottom wire. The blue and orange solid lines represent the wave-packet trajectory in stage I and the black dashed lines represent the wave-packet trajectory in stage II. The purple arrows indicate the direction of motion of the wave packet in stage I and the black arrows indicate the direction of motion of the wave packet in stage II. Shown are (a) the triangular trajectory and (b) the inverse trajectory as well as (b) and (d) enlarged images of them, respectively, close to the splitting wire. The sign h in (a) is the distance from the top wire to the bottom edge of the triangle. The sign b in (b) is the impact parameter. The initial splitting between two wave packets $\Delta z_0 = 2b$. The sign θ_s is the scattering angle. To simplify the calculation, we set $\tau_0 = 0$.

(i) First, we create a small, initial spatial splitting between the two wave packets, potentially using a Stern-Gerlach apparatus.

(ii) Then a microwave pulse is used to map the electron spin state to the nuclear spin state, thus allowing us to ignore the spin-magnetic-field interaction.

(iii) Finally, the wave packets enter the magnetic field generated by the current-carrying wires and are further separated under the diamagnetic repulsion, thus achieving a large superposition size.

The first and second steps are the initial state of the system that we assume. The following analysis is focused on the third step, that is, how to use diamagnetic repulsion to enhance the superposition state. The motion of the wave packet in the magnetic field can be divided into two stages (see Fig. 1).

Stage I. The wave packet is incident parallel to the x axis with an initial velocity v_0 and its trajectory is deflected by the action of the diamagnetic repulsion. Then the wave packet moves towards the top (bottom) wire until the distance from

the x axis reaches a maximum. The spatial distance between the two wave packets also reaches a maximum.

Stage II. The wave-packet trajectory is deflected again near the top (bottom) wire and then returns to its initial position. There are two kinds of trajectories that can go back to their initial positions, the triangle trajectory and the inverse trajectory. For the triangular trajectory, the wave packet returns to its initial position in the second stage by the shortest path [see Fig. 1(a)]. For the inverse trajectory, the wave packet returns to its initial position in the second stage along the path it took in the first stage [see Fig. 1(c)].

IV. ANALYTICAL RESULTS

In the first stage, the motion of a wave packet in the magnetic field can be viewed as the scattering process of a diamagnetic particle in the magnetic field and then solved analytically using polar coordinates. Since the acceleration of the particle is in the radial direction, the equation of motion

can be written as

$$\frac{d^2 r}{dt^2} - r \left(\frac{d\theta}{dt} \right)^2 = \alpha \frac{I^2}{r^3}, \quad (5)$$

where the pole is located at the center of the splitting wire and the polar axis is in the x -axis direction. In this case, θ is the polar angle. The angular momentum of the particle

$$L = |\mathbf{L}| = mr^2 \frac{d\theta}{dt}. \quad (6)$$

By using $d/dt = (L/mr^2)(d/d\theta)$ and noting that the angular momentum is conserved, the initial moment is given by

$$L = mv_0 b, \quad (7)$$

where v_0 is the initial velocity (parallel to the polar axis direction) and b is the vertical distance of the initial position with respect to the polar axis and is called the impact parameter. Substituting Eq. (7) into Eq. (5), we obtain

$$\frac{d^2 u}{d\theta^2} = -ku, \quad (8)$$

where $u = 1/r$ and

$$k = 1 + \alpha \frac{I^2}{v_0^2 b^2}. \quad (9)$$

The solution to Eq. (8) is given by

$$u = C \cos(\sqrt{k}\theta - \theta_0), \quad (10)$$

where C and θ_0 are constants determined by the initial conditions. We will solve for C in Appendix A. Assuming that a particle is incident parallel to the polar axis from infinity and scattered to infinity. When the particle is incident at infinity, $\theta = \pi$, and $u = 0$ we have

$$\sqrt{k}\pi - \theta_0 = \frac{\pi}{2}. \quad (11)$$

Rearranging Eq. (11), we get

$$\theta_0 = (\sqrt{k} - \frac{1}{2})\pi. \quad (12)$$

Here we have taken into account the half period $[-\pi/2, \pi/2]$ of the cosine function. When the particle is scattered to infinity, $\theta = \theta_s$, and $u = 0$ we have

$$\sqrt{k}\theta_s - \theta_0 = -\frac{\pi}{2}. \quad (13)$$

With a bit of rearrangement of Eq. (13) and by combining Eq. (12) we obtain

$$\theta_s = \left(1 - \frac{1}{\sqrt{k}} \right) \pi, \quad (14)$$

which is the scattering angle of the particle. The scattering angle determines the projection of the particle trajectory along the z axis, which is the superposition size we are able to achieve in the experiment.

Next we study what conditions need to be satisfied for the scattering angle to maximize the superposition size. We assume that the collision between the particle and the wire is an elastic collision. Since the mass of the particle is much smaller than the mass of the wire, which we also assume is

clamped to avoid decoherence, the velocity of the particle before and after the collision can be considered unchanged.

In the experimental scheme, the particle has two elastic collisions with the wire. Since the particle is incident from infinity and then returns to infinity, the time for the particle colliding with the wire and thus the change in velocity can be ignored compared to the total time of motion, and the magnitude of the speed of the particle can be treated as a constant. We consider the particle incident parallel to the x axis with an initial velocity v_0 . The initial position of the particle is $(-x_0, b)$ and the value of x_0 is large enough to allow the particle to be approximated as being infinite with respect to the magnetic field generated by the wire.

We set the total time of motion of the particle to be τ . After time τ the particle returns to its initial position and the trajectory length is $v_0\tau$. The trajectory of the particle can be approximated as a triangle with base of length x_0 [see Fig. 1(a)]. The problem now becomes where to locate the vertex of the triangle so that the distance h from the vertex to the base takes its maximum value when the sum of the two sides of the triangle is fixed at $v_0\tau - x_0$. In fact, we are describing the definition of an ellipse. The two focuses of this ellipse are $(-x_0, b)$ and $(0, b)$ and the length of the major axis is $(v_0\tau - x_0)/2$. When the vertex of the triangle is located at the minor axis of this ellipse, the superposition size achieves its maximum value. In this case, the scattering angle θ_s [see Fig. 1(b)] of the particle at the splitting wire satisfies

$$\cos\theta_s = -\frac{x_0}{v_0\tau - x_0}. \quad (15)$$

The negative sign on the right-hand side of Eq. (15) indicates that the particle is incident from the negative x -axis direction. The length of the minor axis

$$\begin{aligned} h &= \frac{v_0\tau - x_0}{2} \sin\theta_s \\ &= \frac{v_0\tau - x_0}{2} \sqrt{1 - \cos^2\theta_s} \\ &= \frac{1}{2} \sqrt{v_0^2\tau^2 - 2v_0x_0\tau}. \end{aligned} \quad (16)$$

By combining the symmetry of the incident trajectories of the two wave packets, the largest superposition size for the triangle trajectory can be written as

$$\Delta Z_{\max T} = 2h = \sqrt{v_0^2\tau^2 - 2v_0x_0\tau}. \quad (17)$$

Letting the scattering angle in Eq. (14) equal the reflection angle in Eq. (15), combined with Eq. (9), we obtain the relationship between the current and the impact parameter and other physical quantities when the superposition size takes its maximum value

$$\frac{I}{b} = \frac{v_0}{\sqrt{\alpha}} \sqrt{\pi^2 \arccos^{-2} \left(\frac{x_0}{v_0\tau - x_0} \right) - 1}. \quad (18)$$

Another way to return the particle to its initial position is to follow along its original path. We set the same initial conditions and the velocity as for the triangular trajectory. In the case of the inverse trajectory, the superposition size takes a maximum value when the reflection angle of the particle

reflected by the splitting wire is $\theta_s = \pi/2$ and then we have

$$\Delta Z_{\max R} = v_0 \tau - 2x_0. \quad (19)$$

We can see that Eqs. (17) and (19) do not include the impact parameter b . This is because we have assumed that the initial splitting between the wave packets is much less than the superposition size we are going to achieve, so the contribution of the impact parameter to the final superposition size can be ignored. Further, if we are given enough time τ then, provided $v_0 \tau \gg x_0 \gg b$, both Eqs. (17) and (19) can be approximated in the compact form

$$\Delta Z_{\max R} \approx v_0 \tau. \quad (20)$$

This simplicity hides the required relationships between the scattering angle, impact parameter, and current. However, it does highlight clearly that the achievable maximum superposition size is determined by the initial conditions and coherence time, not the particle mass.

By setting the scattering angle in Eq. (14) equal to $\pi/2$, we can again obtain the relationship between the current and impact parameter and other physical quantities

$$\frac{I}{b} = v_0 \sqrt{\frac{3}{\alpha}}. \quad (21)$$

To avoid particle collisions with the wire, we need to find the distance of the closest approach d of the particle trajectory to the pole and use this distance as an upper limit on the radius of the wire.

Let us first consider the closest distance d_0 between the particle and the wire when the particle is incident in the direction of the polar axis. From the conservation of energy, we have

$$\frac{1}{2} m v_0^2 = \frac{1}{2} m \alpha \frac{I^2}{d_0^2}. \quad (22)$$

By rearranging Eq. (22) we get

$$d_0^2 = \alpha \frac{I^2}{v_0^2}. \quad (23)$$

This can then be updated to account for a particle incident *parallel* to the polar axis with an impact parameter b . When the particle is nearest to the wire, we have the conservation of energy. Here we have only three of the four variables b , v , d , and I which are independent. The impact parameter b can be determined using the variables v , d , and I ,

$$\frac{1}{2} m v_0^2 = \frac{1}{2} m v^2 + \frac{1}{2} m \alpha \frac{I^2}{d^2}, \quad (24)$$

where v is the velocity of the particle at its nearest point to the wire and d is the distance of the particle trajectory closest to the wire. By combining Eqs. (23) and (24) and simplifying the equation, we obtain

$$\left(\frac{v}{v_0}\right)^2 = 1 - \left(\frac{d_0}{d}\right)^2. \quad (25)$$

Using the conservation of momentum, we can find the impact parameter b in terms of d , v , and v_0 ,

$$L = m v_0 b = m v d, \quad (26)$$

and we have

$$\left(\frac{v}{v_0}\right)^2 = \left(\frac{b}{d}\right)^2. \quad (27)$$

Substituting Eq. (27) into Eq. (25), we get

$$d = \sqrt{b^2 + d_0^2}. \quad (28)$$

Equation (28) is consistent with our intuition that the nearest distance between the particle and the wire increases with increasing impact parameter and current and decreases with increasing initial velocity. As the initial velocity approaches infinity, d_0 approaches 0 and the distance d approaches the impact parameter b .

V. NUMERICAL RESULTS

In this section we solve the wave-packet trajectory numerically using the equation of motion (4). We take into account that the initial conditions satisfy Eq. (18) or (21) to obtain the triangular trajectory or the inverse trajectory. All the three wires are switched on during the movement of the wave packets.

We assume the initial spatial splitting between the two wave packets $\Delta z_0 = 1 \mu\text{m}$ ($b = 0.5 \mu\text{m}$) and the initial velocity $v_0 = 0.01 \text{ m/s}$, which is parallel to the x axis, as shown in Figs. 1(a) and 1(c). Both of these initial conditions could potentially be achieved in a nanocrystal with a mass of 10^{-15} kg by using the Stern-Gerlach apparatus with a magnetic-field gradient of 10^4 T/m [55]. In this paper we focus on how to use the diamagnetic repulsion to further increase the spatial separation between wave packets.

A. Numerical result for the triangular trajectory

We set the current through the splitting wire according to Eq. (18) and then place the top and bottom wires at the minor axis of the ellipse and adjust the current through the wire so that the trajectory of the wave packet forms a triangle back to its initial position. The numerical result of the triangular trajectory is shown in Fig. 1(a). The wave packets are incident from the initial position $(-300, \pm 0.5)$ and the motion time $\tau = 0.1 \text{ s}$. The coordinates of the top and bottom wires are $(-150, \pm 316.5)$. The current through the splitting wire is 0.925 273 A and the current through the top (bottom) wire is 1.57 A . In this case we obtain a maximum superposition size of around $628 \mu\text{m}$. Substituting these initial conditions into Eq. (17) gives a superposition size of around $632 \mu\text{m}$. These two results are close. This indicates that our assumption of a constant motion of the wave packet and a negligible contribution of the impact parameter b to the final superposition size is reasonable.

The closest distance from the triangular trajectory to the splitting wire is $1.392 \text{ 66 } \mu\text{m}$ and the closest distance to the top (bottom) wire is $2.299 \text{ 29 } \mu\text{m}$. By using Eq. (28) we can calculate the closest distance from the wave-packet trajectory to the splitting wire to be $1.392 \text{ 69 } \mu\text{m}$, which agrees well with the numerical results.

If the minimum distance from the wave-packet trajectory to the wire is considered to be the maximum radius of the wire, the minimum current density ρ_{current} required for the

experiment is around $0.15 \text{ A } \mu\text{m}^{-2}$. In the laboratory, current densities of $O(10^0\text{--}10^1) \text{ A } \mu\text{m}^{-2}$ can be achieved using carbon nanotubes and graphene [63–65]. The magnetic field experienced by the wave packet when the triangular trajectory is closest to the wire is around 0.13 T .

B. Numerical results for the inverse trajectory

The numerical analysis of the inverse trajectory is almost the same as that of the triangular trajectory section. Here we set the current through the splitting wire according to Eq. (21), place the top and bottom wires on the $x = -0.5 \text{ } \mu\text{m}$ axis, and adjust the current through the wire so that the trajectory of the wave packet returns to its initial position along its original path.

The numerical result of the inverse trajectory is shown in Fig. 1(c). The wave packets are also incident from the initial position $(-300, \pm 0.5)$ and the motion time $\tau = 0.1 \text{ s}$. The coordinates of the top and bottom wires are $(-0.5, \pm 200)$. The current through the splitting wire is 0.616467 A and the current through the top (bottom) wire is 0.00823 A . In this case we obtain a maximum superposition size of $399.977 \text{ } \mu\text{m}$, which is very close to the result of $400 \text{ } \mu\text{m}$ calculated by Eq. (19). The closest distance from the inverse trajectory to the splitting wire is $0.999996 \text{ } \mu\text{m}$ and the closest distance to the top (bottom) wire is $0.0115617 \text{ } \mu\text{m}$. Following the same discussion as for the triangular trajectory, the minimum current density required for the inverse trajectory scheme is around $19.6 \text{ A } \mu\text{m}^{-2}$. The magnetic field experienced by the wave packet when the inverse trajectory is closest to the wire is around 0.14 T .

Compared to the triangular trajectory, the superposition size achieved by the inverse trajectory is smaller ($400 \text{ } \mu\text{m}$ vs $628 \text{ } \mu\text{m}$ in our case) with the same motion time. The advantage of the inverse trajectory is that when the wave packet returns to its initial position, the velocity of the wave packet is of the same magnitude as that of the initial velocity and in the opposite direction. This means that we can close the trajectories of the wave packets by using an inverse process of creating an initial splitting between the wave packets, for example, via the Stern-Gerlach apparatus. This also helps recover the spin coherence [55].

C. Scaling of superposition size

The most important factor affecting the superposition size is the initial velocity of the wave packet with respect to the wire. According to Eqs. (17) and (19), we can obtain the change in superposition size with initial velocity for the triangular trajectory and the inverse trajectory, as shown in Fig. 2. The superposition sizes that can be achieved for both trajectories are of the same order of magnitude and increase linearly with initial velocity. On the other hand, the larger initial velocity means that we need a larger current density to deflect the trajectory to form a triangular or inverse trajectory.

Combining Eqs. (23) and (28) gives the current density

$$\rho_{\text{current}} = \frac{I}{\pi d^2} = \frac{1}{b} \frac{C_{1,2} v_0^2}{\pi (v_0^2 + \alpha C_{1,2}^2)}, \quad (29)$$

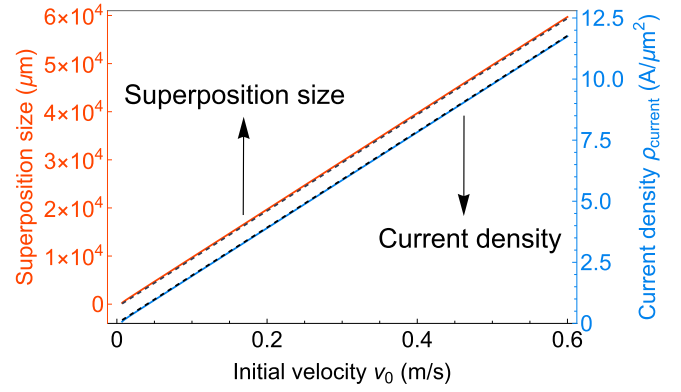


FIG. 2. Size of the superposition and the required current density with regard to the initial velocity. The upper red solid line and black dashed line correspond to the superposition size that can be achieved for the triangular trajectory and the inverse trajectory for different initial velocities, respectively. The lower blue solid line and black dashed line correspond to the current density required to form a triangular trajectory and an inverse trajectory for different initial velocities, respectively. Here we have set the impact parameter $b = 0.5 \text{ } \mu\text{m}$, the initial coordinate $-x_0 = -300 \text{ } \mu\text{m}$, and the motion time $\tau = 0.1 \text{ s}$.

where $C_1 = I/b$ corresponds to the triangular trajectory [see Eq. (18)] and $C_2 = I/b$ corresponds to the inverse trajectory [see Eq. (21)]. Figure 2 also shows the change in current density with initial velocity. We can see that when the initial velocity is large enough, the current density corresponding to the triangular trajectory and the inverse trajectory changes linearly with the initial velocity and the curves almost coincide. If we consider that the initial velocity and motion time of the wave packet are determined, then C_1 and C_2 are constants and the current density is inversely proportional to the initial splitting between wave packets, that is, for smaller initial splitting, we need larger current density to achieve the same superposition size.

D. Comparing schemes for creating spatial superposition

Here we briefly compare the different schemes for creating the spatial superposition. The larger the mass and size of the superposition state and the longer the coherence time, the more likely it is to induce decoherence due to thermal radiation, gas collisions, and other noise, e.g., fluctuations in electromagnetic fields and phonon excitations [5,6,15,23–25,66–68]. Different combinations of (a) small mass (approximately 10^{-25} kg , ^{87}Rb), large superposition size (approximately 54 cm), and short coherence time (approximately 2 s) [69]; (b) small mass (approximately 10^{-25} kg , ^{133}Cs), small superposition size (approximately $4 \text{ } \mu\text{m}$), and long coherence time (approximately 20 s) [70]; and (c) large mass (approximately 10^{-23} kg , oligoporphyrins), small superposition size (approximately 100 nm), and short coherence time (approximately 8 ms) [71] have been implemented in the laboratory recently. However, the methods of light-pulse and matter-wave diffraction used in schemes (a)–(c) are difficult to apply to larger masses of superposition states (e.g., $10^{-17}\text{--}10^{-14} \text{ kg}$) on account of internal heating and too

short de Broglie wavelengths [66]. In Ref. [53] a full-loop Stern-Gerlach interferometer was realized using magnetic-field–spin coupling for a mass of approximately 10^{-25} kg (^{87}Rb), a superposition size of approximately $2\ \mu\text{m}$, and a coherence time of approximately 4 ms. The advantage of this method is that it can potentially be used to create large spatial superposition ($1\text{--}10\ \mu\text{m}$) with large masses ($10^{-17}\text{--}10^{-14}$ kg) [53–55]. However, since the effect of using magnetic-field–spin coupling to separate wave packets is inversely proportional to mass, this limits the superposition size that can be achieved for macroscopic superposition. Our solution is to increase a small superposition size (e.g., $1\ \mu\text{m}$) to the order of $10^2\ \mu\text{m}$ by mass-independent diamagnetic repulsion effects [Eq. (4)]. We note that recently there have been some novel ideas to enhance entanglement signals as well, for example, by coupling a small-mass two-level system to a massive mediator oscillator to amplify the entanglement phase [72] or by the amplified-weak-value phenomenon in two-setting Einstein-Podolsky-Rosen steering to increase the sensitivity to weak entanglement signals [73]. Interestingly, in principle, our scheme can be combined with those in [72,73] to significantly improve the sensitivity of the detection of entangled signals.

VI. CONCLUSION AND DISCUSSION

In this paper we proposed a mass-independent scheme to obtain large spatial superposition. We analytically and numerically studied two possible trajectories, which we call the triangular trajectory and the inverse trajectory. We found that given an initial spatial splitting $\Delta z_0 = 1\ \mu\text{m}$, an initial velocity $v_0 = 0.01\ \text{m/s}$, and total time $\tau = 0.1\ \text{s}$, the maximum superposition size achievable with the triangular trajectory is $632\ \mu\text{m}$ and that for the inverse trajectory is $400\ \mu\text{m}$. This represents a 400–632 times enhancement on the initial splitting and is completely independent of the mass used.

For both the triangular and the inverse trajectories, we chose to require the wave packets to return approximately to their initial positions. In principle, however, as long as the spatial separation between the wave packets is less than or equal to the initial splitting, we can likely recombine the trajectories of the two wave packets coherently via the Stern-Gerlach setup (see [55]).

It may not be necessary to accelerate the nanocrystal to the desired initial velocity by the Stern-Gerlach apparatus. We could, for example, consider the nanocrystal falling in a gravitational field while the wires remain stationary in the gravitational field. Since the gravitational acceleration is about $9.8\ \text{m/s}^2$, we can easily achieve a large relative velocity between the nanocrystal and the wire and thus realize the same scattering process. Details of this construction are left for future work.

In addition, further considerations will be required, depending on the method of generating the initial splitting and final interference. For example, a high-precision controlled magnetic field is needed to finally recover spin coherence [74] if using a Stern-Gerlach interferometer. While not considered in great detail here, this spin coherence has been studied elsewhere [75–79]. Indeed, spin coherence times have been gradually improving (approaching 1 s [75,76], even 30 s

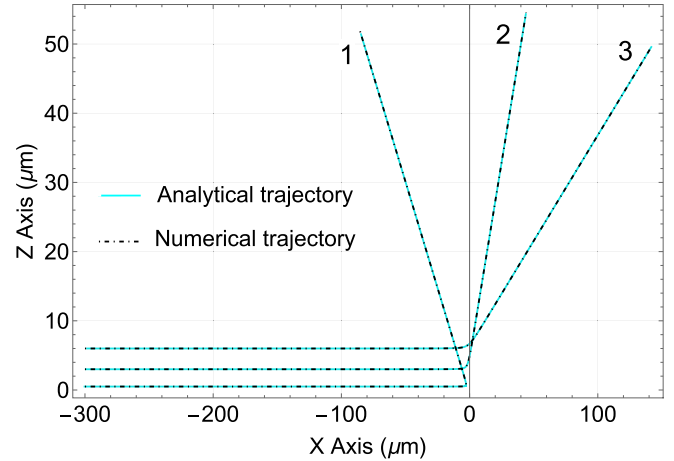


FIG. 3. Comparison of the analytical and numerical trajectories of the particle in the magnetic field. The blue solid line is the analytical trajectory and the black dot-dashed line is the numerical trajectory. Trajectories 1, 2, and 3 correspond to impact parameters of 0.5, 3, and $6\ \mu\text{m}$, respectively. These three trajectories correspond to particles with an initial velocity of $0.01\ \text{m/s}$. The splitting wire is located at the origin and the current through the wire is $2\ \text{A}$.

[77,78]); adapting these to nanocrystals remains an open problem, but there are no fundamental constraints [79]. The spatial coherence times can be made $100\ \text{s}$ (see [5,15,16]). There are other very important challenges, achieving pressures, temperatures, distances from other sources, and fluctuations [15]. In addition to these, we will need to ensure that we can close the interferometer loop [74]. This requires the position, the momentum, and the spin direction to be aligned (see [59]). Furthermore, we will need to analyze the spin coherence including the rotation of the nanocrystal if the NV center is not at the center of the nanocrystal [59] and the excitations of the phonons [60]. However, such considerations are left for further study. Indeed, given this diamagnetic enhancement does not itself require any spin-based manipulation, there may be other, simpler candidate systems for creating (and closing) the initial small spatial splitting which does not concern itself with such issues. However, it will likely require similar efforts to ensure coherent interference is possible.

ACKNOWLEDGMENTS

We would like to thank Ron Folman for helpful discussions. R.Z. was supported by a China Scholarship Council fellowship. R.J.M. was supported by the Australian Research Council under the Centre of Excellence for Quantum Computation and Communication Technology (Grant No. CE170100012). A.M. would like to thank Institute for Advanced Study Princeton for their kind hospitality during the completion of this paper.

APPENDIX A: SOLVING AMPLITUDE C

To solve for the constant C in Eq. (10), we consider a point on the incident trajectory which is at a distance b from the

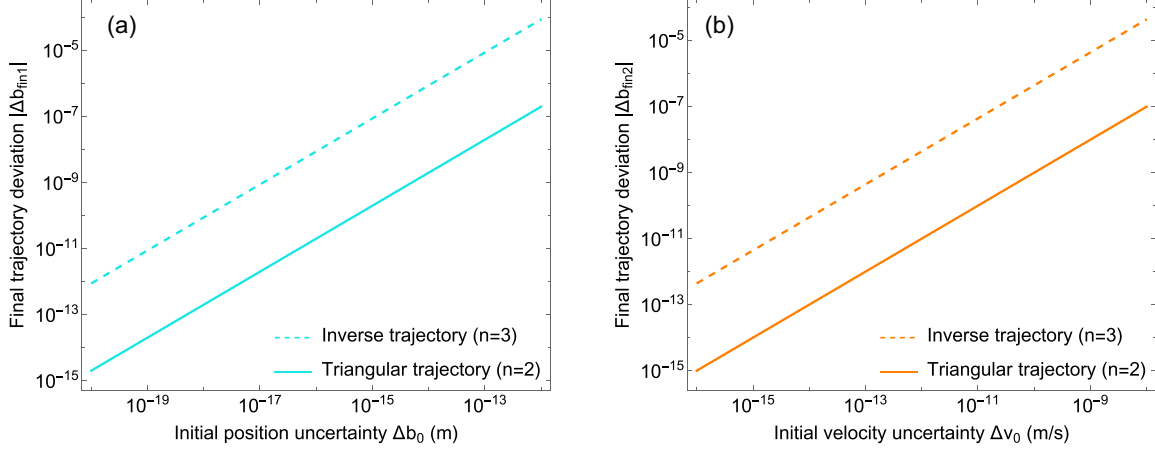


FIG. 4. Relation between the deviation in the final trajectory and the uncertainty of the initial (a) position and (b) velocity. The blue and orange dashed lines correspond to the inverse trajectories. The blue and orange solid lines correspond to the triangular trajectories. We have set $\theta_s = 3\pi/4$, $b = 0.5 \mu\text{m}$, and $L = 300 \mu\text{m}$.

polar axis and satisfies $\sqrt{k}bu \ll 1$. Then we have

$$\begin{aligned}
 u &= C \cos\{\sqrt{k}[\pi - \arcsin(bu)] - \theta_0\} \\
 &\approx C \cos[\sqrt{k}(\pi - bu) - \theta_0] \\
 &= C \cos(\sqrt{k}\pi - \theta_0)\cos(\sqrt{k}bu) \\
 &\quad + C \sin(\sqrt{k}\pi - \theta_0)\sin(\sqrt{k}bu) \\
 &= C \sin(\sqrt{k}bu) \\
 &\approx C\sqrt{k}bu,
 \end{aligned} \tag{A1}$$

where the relation $\sqrt{k}\pi - \theta_0 = \pi/2$ is used. The constant C can be obtained by solving Eq. (A1), which is

$$C = \frac{1}{\sqrt{k}b}. \tag{A2}$$

Combining Eqs. (8), (12), and (A3), we can finally obtain the analytical trajectory of the particle as

$$r = \frac{\sqrt{k}b}{\cos[\sqrt{k}\theta - (\sqrt{k} - \frac{1}{2})\pi]}. \tag{A3}$$

We can solve the trajectory of the particle numerically using Eq. (4) and then compare it with the analytical solution in Eq. (A3), as shown in Fig. 3. The analytical results fit well with the numerical results.

APPENDIX B: UNCERTAINTIES IN THE PARAMETERS

Here we briefly discuss the effect of uncertainties in the initial position and velocity on the accuracy of the final position. Using the expression for the scattering angle, Eq. (14), to differentiate the impact parameter and initial velocity gives

$$\Delta\theta_{si} = -A \frac{\Delta b_0}{b} \tag{B1}$$

and

$$\Delta\theta_{sv} = -A \frac{\Delta v_0}{v_0}, \tag{B2}$$

where

$$A = \frac{k-1}{k^{3/2}}\pi. \tag{B3}$$

The expression for k is given by Eq. (9).

To simplify the discussion, we assume that the impact parameter is b , the scattering angle is $3\pi/4$ for each scattering, and the distance from the initial position to the wire and from the splitting wire to the top (bottom) wire is L . With the help of Eqs. (B1) and (B2) we can solve the deviation in the trajectories, when the wave packet returns to its initial position

$$|\Delta b_{\text{fin1}}| = A^n \frac{\Delta b_0}{b^n} L^n \tag{B4}$$

and

$$|\Delta b_{\text{fin2}}| = A^n \frac{\Delta v_0}{v_0 b^{n-1}} L^n. \tag{B5}$$

Here Δb_{fin1} and Δb_{fin2} are trajectory deviations caused by inaccuracies in the initial position and initial velocity, respectively. The superscript n represents the number of scatterings between the diamond and the wire; $n = 2$ for the triangular trajectory and $n = 3$ for the inverse trajectory. The final trajectory deviation with the initial position and the velocity uncertainty is shown in Fig. 4. For the same initial position or velocity uncertainty, the deviation of the inverse trajectory at the final position is approximately three orders of magnitude greater than the deviation of the triangular trajectory (we have fixed $L = 300 \mu\text{m}$).

It is worth noting that the uncertainty in the initial position and the velocity here is not the width of the position and momentum of the wave packet. The uncertainty here refers to the environmental perturbation of the wave packet position and momentum, which can be much smaller than the position and momentum width of the wave packet. For example, Margalit *et al.* used Stern-Gerlach interferometry to separate ^{87}Rb atoms and eventually recover spin coherence by precisely controlling the current and pulse timing [52]. The condition for recovering spin coherence is that the classical uncertainties in position and momentum are much smaller than the quantum uncertainties [74].

- [1] F. Dyson, Is a graviton detectable? *Int. J. Mod. Phys. A* **28**, 1330041 (2013).
- [2] J. Martin and V. Vennin, Obstructions to Bell CMB experiments, *Phys. Rev. D* **96**, 063501 (2017).
- [3] A. Ashoorioon, P. S. Bhupal Dev, and A. Mazumdar, Implications of purely classical gravity for inflationary tensor modes, *Mod. Phys. Lett. A* **29**, 1450163 (2014).
- [4] A. Addazi *et al.*, Quantum gravity phenomenology at the dawn of the multi-messenger era—A review, *Prog. Part. Nucl. Phys.* **125**, 103948 (2022).
- [5] S. Bose, A. Mazumdar, G. W. Morley, H. Ulbricht, M. Toroš, M. Paternostro, A. A. Geraci, P. F. Barker, M. S. Kim, and G. Milburn, Spin Entanglement Witness for Quantum Gravity, *Phys. Rev. Lett.* **119**, 240401 (2017).
- [6] R. J. Marshman, A. Mazumdar, and S. Bose, Locality and entanglement in table-top testing of the quantum nature of linearized gravity, *Phys. Rev. A* **101**, 052110 (2020).
- [7] S. Bose, A. Mazumdar, M. Schut, and M. Toroš, Mechanism for the quantum natured gravitons to entangle masses, *Phys. Rev. D* **105**, 106028 (2022).
- [8] C. Marletto and V. Vedral, Gravitationally Induced Entanglement between Two Massive Particles is Sufficient Evidence of Quantum Effects in Gravity, *Phys. Rev. Lett.* **119**, 240402 (2017).
- [9] C. Marletto and V. Vedral, Witnessing nonclassicality beyond quantum theory, *Phys. Rev. D* **102**, 086012 (2020).
- [10] M. Christodoulou and C. Rovelli, On the possibility of laboratory evidence for quantum superposition of geometries, *Phys. Lett. B* **792**, 64 (2019).
- [11] M. Christodoulou, A. Di Biagio, M. Aspelmeyer, Č. Brukner, C. Rovelli, and R. Howl, Locally mediated entanglement through gravity from first principles, [arXiv:2202.03368](https://arxiv.org/abs/2202.03368)
- [12] T. D. Galley, F. Giacomini, and J. H. Selby, A no-go theorem on the nature of the gravitational field beyond quantum theory, *Quantum* **6**, 779 (2022).
- [13] D. Biswas, S. Bose, A. Mazumdar, and M. Toroš, Gravitational optomechanics: Photon-matter entanglement via graviton exchange, [arXiv:2209.09273](https://arxiv.org/abs/2209.09273).
- [14] D. Carney, Newton, entanglement, and the graviton, *Phys. Rev. D* **105**, 024029 (2022).
- [15] T. W. van de Kamp, R. J. Marshman, S. Bose, and A. Mazumdar, Quantum gravity witness via entanglement of masses: Casimir screening, *Phys. Rev. A* **102**, 062807 (2020).
- [16] M. Toroš, T. W. van de Kamp, R. J. Marshman, M. S. Kim, A. Mazumdar, and S. Bose, Relative acceleration noise mitigation for nanocrystal matter-wave interferometry: Applications to entangling masses via quantum gravity, *Phys. Rev. Res.* **3**, 023178 (2021).
- [17] R. Penrose, On gravity's role in quantum state reduction, *Gen. Relativ. Gravit.* **28**, 581 (1996).
- [18] L. Diósi, Continuous quantum measurement and Itô formalism, *Phys. Lett. A* **129**, 419 (1988).
- [19] P. Pearle, Combining stochastic dynamical state-vector reduction with spontaneous localization, *Phys. Rev. A* **39**, 2277 (1989).
- [20] A. Bassi, K. Lochan, S. Satin, T. P. Singh, and H. Ulbricht, Models of wave-function collapse, underlying theories, and experimental tests, *Rev. Mod. Phys.* **85**, 471 (2013).
- [21] S. Nimmrichter and K. Hornberger, Macroscopicity of Mechanical Quantum Superposition States, *Phys. Rev. Lett.* **110**, 160403 (2013).
- [22] S. Bose, A. Mazumdar, M. Schut, and M. Toroš, Entanglement witness for the weak equivalence principle, [arXiv:2203.11628](https://arxiv.org/abs/2203.11628).
- [23] O. Romero-Isart, Quantum superposition of massive objects and collapse models, *Phys. Rev. A* **84**, 052121 (2011).
- [24] O. Romero-Isart, A. C. Pflanzer, F. Blaser, R. Kaltenbaek, N. Kiesel, M. Aspelmeyer, and J. I. Cirac, Large Quantum Superpositions and Interference of Massive Nanometer-Sized Objects, *Phys. Rev. Lett.* **107**, 020405 (2011).
- [25] O. Romero-Isart, M. L. Juan, R. Quidant, and J. I. Cirac, Toward quantum superposition of living organisms, *New J. Phys.* **12**, 033015 (2010).
- [26] J. Tilly, R. J. Marshman, A. Mazumdar, and S. Bose, Qudits for witnessing quantum-gravity-induced entanglement of masses under decoherence, *Phys. Rev. A* **104**, 052416 (2021).
- [27] M. Schut, J. Tilly, R. J. Marshman, S. Bose, and A. Mazumdar, Improving resilience of quantum-gravity-induced entanglement of masses to decoherence using three superpositions, *Phys. Rev. A* **105**, 032411 (2022).
- [28] S. Rijavec, M. Carlesso, A. Bassi, V. Vedral, and C. Marletto, Decoherence effects in non-classicality tests of gravity, *New J. Phys.* **23**, 043040 (2021).
- [29] D. Carney, P. C. E. Stamp, and J. M. Taylor, Tabletop experiments for quantum gravity: A user's manual, *Class. Quantum Gravity* **36**, 034001 (2019).
- [30] R. J. Marshman, A. Mazumdar, G. W. Morley, P. F. Barker, S. Hoekstra, and S. Bose, Mesoscopic interference for metric and curvature & gravitational wave detection, *New J. Phys.* **22**, 083012 (2020).
- [31] P. F. Barker, S. Bose, R. J. Marshman, and A. Mazumdar, Entanglement based tomography to probe new macroscopic forces, *Phys. Rev. D* **106**, L041901 (2022).
- [32] J. M. McGuirk, G. T. Foster, J. B. Fixler, M. J. Snadden, and M. A. Kasevich, Sensitive absolute-gravity gradiometry using atom interferometry, *Phys. Rev. A* **65**, 033608 (2002).
- [33] S. Dimopoulos, P. W. Graham, J. M. Hogan, and M. A. Kasevich, General relativistic effects in atom interferometry, *Phys. Rev. D* **78**, 042003 (2008).
- [34] P. Asenbaum, C. Overstreet, T. Kovachy, D. D. Brown, J. M. Hogan, and M. A. Kasevich, Phase Shift in an Atom Interferometer due to Spacetime Curvature across its Wave Function, *Phys. Rev. Lett.* **118**, 183602 (2017).
- [35] M. Arndt, O. Nairz, J. Vos-Andreae, C. Keller, G. van der Zouw, and A. Zeilinger, Wave-particle duality of C_{60} molecules, *Nature (London)* **401**, 680 (1999).
- [36] S. Gerlich, S. Eibenberger, M. Tomandl, S. Nimmrichter, K. Hornberger, P. J. Fagan, J. Tüxen, M. Mayor, and M. Arndt, Quantum interference of large organic molecules, *Nat. Commun.* **2**, 263 (2011).
- [37] S. Bose, K. Jacobs, and P. L. Knight, A Scheme to probe the decoherence of a macroscopic object, *Phys. Rev. A* **59**, 3204 (1999).
- [38] P. Sekatski, M. Aspelmeyer, and N. Sangouard, Macroscopic Optomechanics from Displaced Single-Photon Entanglement, *Phys. Rev. Lett.* **112**, 080502 (2014).
- [39] J. M. Hogan, D. Johnson, and M. A. Kasevich, in *Atom Optics and Space Physics*, Proceedings of the International School of Physics "Enrico Fermi," Course CLXVIII, Varenna, 2007,

- edited by E. Arimondo, W. Ertmer, and W. P. Schleich (IOS, Amsterdam, 2008).
- [40] C. Wan, M. Scala, G. W. Morley, ATM. A. Rahman, H. Ulbricht, J. Bateman, P. F. Barker, S. Bose, and M. S. Kim, Free Nano-Object Ramsey Interferometry for Large Quantum Superpositions, *Phys. Rev. Lett.* **117**, 143003 (2016).
- [41] M. Scala, M. S. Kim, G. W. Morley, P. F. Barker, and S. Bose, Matter-Wave Interferometry of a Levitated Thermal Nano-Oscillator Induced and Probed by a Spin, *Phys. Rev. Lett.* **111**, 180403 (2013).
- [42] Z.-q. Yin, T. Li, X. Zhang, and L. M. Duan, Large quantum superpositions of a levitated nanodiamond through spin-optomechanical coupling, *Phys. Rev. A* **88**, 033614 (2013).
- [43] J. Clarke and M. R. Vanner, Growing macroscopic superposition states via cavity quantum optomechanics, *Quantum Sci. Technol.* **4**, 014003 (2019).
- [44] B. D. Wood, S. Bose, and G. W. Morley, Spin dynamical decoupling for generating macroscopic superpositions of a free-falling nanodiamond, *Phys. Rev. A* **105**, 012824 (2022).
- [45] R. Kaltenbaek, M. Aspelmeyer, P. F. Barker, A. Bassi, J. Bateman, K. Bongs, S. Bose, C. Braxmaier, Č. Brukner, B. Christophe *et al.*, Macroscopic quantum resonators (MAQRO): 2015 update, *EPJ Quantum Technol.* **3**, 5 (2016).
- [46] H. Pino, J. Prat-Camps, K. Sinha, B. P. Venkatesh, and O. Romero-Isart, On-chip quantum interference of a superconducting microsphere, *Quantum Sci. Technol.* **3**, 025001 (2018).
- [47] O. Romero-Isart, Coherent inflation for large quantum superpositions of levitated microspheres, *New J. Phys.* **19**, 123029 (2017).
- [48] R. Kaltenbaek, G. Hechenblaikner, N. Kiesel, O. Romero-Isart, K. C. Schwab, U. Johann, and M. Aspelmeyer, Macroscopic quantum resonators (MAQRO), *Exp. Astron.* **34**, 123 (2012).
- [49] M. Arndt and K. Hornberger, Testing the limits of quantum mechanical superpositions, *Nat. Phys.* **10**, 271 (2014).
- [50] S. Machluf, Y. Japha, and R. Folman, Coherent Stern-Gerlach momentum splitting on an atom chip, *Nat. Commun.* **4**, 2424 (2013).
- [51] O. Amit, Y. Margalit, O. Dobkowski, Z. Zhou, Y. Japha, M. Zimmermann, M. A. Efremov, F. A. Narducci, E. M. Rasel, W. P. Schleich, and R. Folman, T^3 Stern-Gerlach Matter-Wave Interferometer, *Phys. Rev. Lett.* **123**, 083601 (2019).
- [52] Y. Margalit, Z. Zhou, O. Dobkowski, Y. Japha, D. Rohrlach, S. Moukouri, and R. Folman, Realization of a complete Stern-Gerlach interferometer, [arXiv:1801.02708](https://arxiv.org/abs/1801.02708).
- [53] Y. Margalit, O. Dobkowski, Z. Zhou, O. Amit, Y. Japha, S. Moukouri, D. Rohrlach, A. Mazumdar, S. Bose, C. Henkel, and R. Folman, Realization of a complete Stern-Gerlach interferometer: Toward a test of quantum gravity, *Sci. Adv.* **7**, eabg2879 (2021).
- [54] R. J. Marshman, A. Mazumdar, R. Folman, and S. Bose, Constructing nano-object quantum superpositions with a Stern-Gerlach interferometer, *Phys. Rev. Res.* **4**, 023087 (2022).
- [55] R. Zhou, R. J. Marshman, S. Bose, and A. Mazumdar, Catapulting towards massive and large spatial quantum superposition, *Phys. Rev. Res.* **4**, 043157 (2022).
- [56] J. S. Pedernales, G. W. Morley, and M. B. Plenio, Motional Dynamical Decoupling for Interferometry with Macroscopic Particles, *Phys. Rev. Lett.* **125**, 023602 (2020).
- [57] A. A. Wood, R. M. Goldblatt, R. E. Scholten, and A. M. Martin, Quantum control of nuclear-spin qubits in a rapidly rotating diamond, *Phys. Rev. Res.* **3**, 043174 (2021).
- [58] B. A. Stickler, K. Hornberger, and M. S. Kim, Quantum rotations of nanoparticles, *Nat. Rev. Phys.* **3**, 589 (2021).
- [59] Y. Japha and R. Folman, Role of rotations in Stern-Gerlach interferometry with massive objects, [arXiv:2202.10535](https://arxiv.org/abs/2202.10535).
- [60] C. Henkel and R. Folman, Internal decoherence in nano-object interferometry due to phonons, *AVS Quantum Sci.* **4**, 025602 (2022).
- [61] J. H. N. Loubser and J. A. van Wyk, Electron spin resonance in the study of diamond, *Rep. Prog. Phys.* **41**, 1201 (1978).
- [62] F. Shi, X. Kong, P. Wang, F. Kong, N. Zhao, R.-B. Liu, and J. Du, Sensing and atomic-scale structure analysis of single nuclear-spin clusters in diamond, *Nat. Phys.* **10**, 21 (2014).
- [63] Z. Yao, C. L. Kane, and C. Dekker, High-Field Electrical Transport in Single-Wall Carbon Nanotubes, *Phys. Rev. Lett.* **84**, 2941 (2000).
- [64] B. Q. Wei, R. Vajtai, and P. M. Ajayan, Reliability and current carrying capacity of carbon nanotubes, *Appl. Phys. Lett.* **79**, 1172 (2001).
- [65] R. Murali, Y. Yang, K. Brenner, T. Beck, and J. D. Meindl, Breakdown current density of graphene nanoribbons, *Appl. Phys. Lett.* **94**, 243114 (2009).
- [66] C. Gonzalez-Ballester, M. Aspelmeyer, L. Novotny, R. Quidant, and O. Romero-Isart, Levitodynamics: Levitation and control of microscopic objects in vacuum, *Science* **374**, eabg3027 (2021).
- [67] K. Hornberger, J. E. Sipe, and M. Arndt, Theory of decoherence in a matter wave Talbot-Lau interferometer, *Phys. Rev. A* **70**, 053608 (2004).
- [68] K. Sinha and P. W. Milonni, Dipoles in blackbody radiation: Momentum fluctuations, decoherence, and drag force, *J. Phys. B* **55**, 204002 (2022).
- [69] T. Kovachy, P. Asenbaum, C. Overstreet, C. A. Donnelly, S. M. Dickerson, A. Sugarbaker, J. M. Hogan, and M. A. Kasevich, Quantum superposition at the half-metre scale, *Nature (London)* **528**, 530 (2015).
- [70] V. Xu, M. Jaffe, C. D. Panda, S. L. Kristensen, L. W. Clark, and H. Müller, Probing gravity by holding atoms for 20 seconds, *Science* **366**, 745 (2019).
- [71] Y. Y. Fein, P. Geyer, P. Zwick, F. Kiałka, S. Pedalino, M. Mayor, S. Gerlich, and M. Arndt, Quantum superposition of molecules beyond 25 kDa, *Nat. Phys.* **15**, 1242 (2019).
- [72] J. S. Pedernales, K. Streltsov, and M. B. Plenio, Enhancing Gravitational Interaction between Quantum Systems by a Massive Mediator, *Phys. Rev. Lett.* **128**, 110401 (2022).
- [73] T. Feng and V. Vedral, Amplification of gravitationally induced entanglement, *Phys. Rev. D* **106**, 066013 (2022).
- [74] J. Schwinger, M. O. Scully, and B. G. Englert, Is spin coherence like Humpty-Dumpty? II. General theory, *Z. Phys. D* **10**, 135 (1988).
- [75] N. Bar-Gill, L. M. Pham, A. Jarmola, D. Budker, and R. L. Walsworth, Solid-state electronic spin coherence time approaching one second, *Nat. Commun.* **4**, 1743 (2013).
- [76] M. H. Abobeih, J. Cramer, M. A. Bakker, N. Kalb, M. Markham, D. J. Twitchen, and T. H. Taminau, One-second coherence for a single electron spin coupled to a

- multi-qubit nuclear-spin environment, *Nat. Commun.* **9**, 2552 (2018).
- [77] J. T. Muhonen, J. P. Dehollain, A. Laucht, F. E. Hudson, R. Kalra, T. Sekiguchi, K. M. Itoh, D. N. Jamieson, J. C. McCallum, A. S. Dzurak, and A. Morello, Storing quantum information for 30 seconds in a nanoelectronic device, *Nat. Nanotechnol.* **9**, 986 (2014).
- [78] D. Farfurnik, A. Jarmola, L. M. Pham, Z. H. Wang, V. V. Dobrovitski, R. L. Walsworth, D. Budker, and N. Bar-Gill, Optimizing a dynamical decoupling protocol for solid-state electronic spin ensembles in diamond, *Phys. Rev. B* **92**, 060301(R) (2015).
- [79] H. S. Knowles, D. M. Kara, and M. Atatüre, Observing bulk diamond spin coherence in high-purity nanodiamonds, *Nat. Mater.* **13**, 21 (2014).